Pre-earthquake Electric Field Disturbances and Interference Analysis Based on CSES-01 Satellite Observations

Jianping Huang[1,2], Junjie Song[1,2], Zhong Li[2*], Wenjing Li[1], Hengxin Lu[1], Xingsu Li[2], Yumeng Huo[2], Ruiqi Yang[2]

[1]National Institute of Natural Hazards, Ministry of Emergency Management, Beijing, 100085, China

[2]Institute of Intelligent Emergency Information Processing, Institute of Disaster Prevention, Langfang, 065201, China

Correspondence to: Zhong Li (lizhong@cidp.edu.cn)

Abstract. Anomalous electromagnetic phenomena in the ionosphere before and after seismic activity have been identified as potential indicators for earthquake early warning. Data from the CSES-01 satellite were analyzed using the STL decomposition method to break down electric field time series into longitudinal, latitudinal, and residual components. The longitudinal and latitudinal components reveal the electric field's double periodicity, characterized by a V-shape from south to north and a bimodal shape from east to west. After isolating conventional periodic disturbances with a strength of 0.87, unconventional disturbances in the residual component were examined to identify seismic precursor anomalies. Electric field power density disturbances associated with the May 11, 2023, Tonga Islands magnitude 7.6 earthquake were extracted. Multiple significant anomalies in the ionospheric electric field were detected within 20 days prior to the earthquake: an initial anomaly with a C-value exceeding 3.5 appeared 20 days before; a persistent anomaly with a peak C-value of 3.9 occurred 13 to 11 days prior; a sharp increase to a peak C-value of 4.4, three times the standard deviation, was observed seven days prior; disturbances decreased until a resurgence four days prior, with a peak C-value of 3.5 lasting two days; the C-value returned to baseline one day before the earthquake. The STL-C method effectively differentiates various causal disturbances in the ionospheric electric field, offering novel approaches and insights for studying seismic precursors.

1 Introduction

The ionosphere plays a crucial role in the Earth's atmospheric structure. Situated at an altitude of approximately 60 to 1,000 kilometers above the Earth's surface, this layer is characterized by a high degree of ionization, containing numerous ions and free electrons. Its uniqueness lies in its ability to reflect radio and other electromagnetic waves, fundamentally impacting global communication systems and radar detection technologies. The ionosphere's state is influenced by various external factors, including geomagnetic effects, solar activity, diurnal and seasonal variations, and natural phenomena such as magnetic storms and earthquakes. Diurnal variations in the ionosphere primarily manifest as differences in ionization levels between daytime and nighttime, caused by the increased solar radiation during the day. Seasonal variations relate to changes in the Earth's orbital position, affecting the angle and duration of solar radiation incidence. Although solar activity is considered the primary source of ionospheric variability in ionospheric physics, recent studies have established that significant effects on the ionosphere, such as those from volcanic eruptions and magnetic storms, are substantial(Sokolov et al., 2011; Pulinets et al., 2022). Strong earthquakes are also recognized as important perturbation sources, as documented in numerous publications(Silina et al., 2001; Astafyeva et al., 2013). During the preparation and occurrence of earthquakes, the ionosphere in and around the source region exhibits varying degrees of electromagnetic phenomena, typically appearing days or hours before the onset of an earthquake, making them highly sensitive precursor indicators for earthquake prediction(Sarkar et al., 2007).

Since the 1960s, the phenomenon of pre-seismic ionospheric disturbances has garnered extensive attention from scientists. As early as March 28, 1964, following the Alaska earthquake, Leonard and Barnes (1965) observed two forms of ionospheric disturbances at four ionospheric stations and found that the disturbances' nature depended on the distance between the observatory

and the earthquake's epicenter. In the same year, Baker (1965) observed irregular disturbances in various high-frequency bands
40 (10 MHz, 5 MHz, and 4 MHz) before and after the main shock. This discovery sparked significant interest among scientists in detecting earthquakes within the near-Earth spatial range, leading to studies exploring the relationship between earthquakes and ionospheric variations using both ground-based and space-based observations. Using data from the Sugadaira Space Radio Observatory (SRO) in Japan, Gokhberg and Morgounov (1982) recorded electromagnetic signals with amplitudes 15 dB higher than usual prior to the mainshock. Similarly, Larkina et al. (1983), using data from Intercosmos 19, found an unusual increase in
45 VLF signal strength in the F-region of the ionosphere both before and hours after the earthquake. Parrot and Mogilevsky (1989), using data from the geosynchronous satellite GEOS 2 and the polar satellite Aureol 3, discovered a significant increase in VLF signal strength in the F-region of the ionosphere. They also found that earthquakes can cause electromagnetic disturbances in the ionosphere, manifesting as electromagnetic wave disturbances and electron density enhancements in the Es layer. Chmyrev et al. (1989), using data from the Intercosmos Bulgaria 1300 satellite, studied an earthquake on January 21, 1982, and found significant
50 electrostatic and magnetic field disturbances over the epicenter within the first ten minutes. Serebryakova et al. (1990) studied ELF electromagnetic radiation detected by the low-orbiting satellites COSMOS 1809 and AUREOL-3 as they passed over the seismic region. They found strong electromagnetic radiation in the frequency band below 450 Hz in the magnetic crust parameters corresponding to the earthquake's epicenter, persisting throughout the region of seismic activity.

Since then, numerous studies have focused on seismic ionospheric disturbances, with scholars deepening their understanding of
55 the seismic ionosphere's response mechanisms through various observational means and data analysis methods. As short-term precursors to earthquakes, seismic electromagnetic phenomena primarily manifest within days to hours before seismic events (Chen et al., 2022; Fan et al., 2010). Bhattacharya et al. (2009) found that Ultra Low Frequency (ULF), Extremely Low Frequency (ELF), and Very Low Frequency (VLF) electromagnetic waves, due to their greater penetration depth and reduced attenuation, are observed more prominently during seismic events. Since the 20th century, both ground-based and satellite
60 observations have demonstrated that a broad spectrum of electromagnetic (EM) signals can be detected in the vicinity of major earthquakes (Pulinets, 2004). These EM disturbances persist for a longer duration on the ground, whereas they are consistently observed in space within days or even hours before an earthquake (Shen et al., 2018).

On February 2, 2018, China's first space-based platform for three-dimensional earthquake observation, the pilot satellite of the National Geophysical Field Exploration Satellite Project, CSES-01, was successfully launched, playing a significant role in
65 global space environment monitoring. The satellite's primary mission is to construct a space-based experimental platform for monitoring key physical quantities, such as global electromagnetic fields, electromagnetic waves, ionospheric ions, and energetic particles (Zhima et al., 2022; Martucci et al., 2022). This enables quasi-real-time monitoring and tracking of China and its neighboring regions, as well as research on electromagnetic information for earthquakes of magnitude 7 or above globally and magnitude 6 or above in China(Li et al., 2020; Marchetti et al., 2020; Li et al., 2022). Additionally, it aims to
70 explore the characteristics and mechanisms of ionospheric response to earthquakes(Chen et al., 2023). In this study, night-side electric field data collected by the CSES-01 satellite before and after the 7.6 magnitude earthquake in the Tonga Islands on May 11, 2023, are analyzed. Using a time series decomposition algorithm, cyclic disturbances affecting the observed ionospheric effects in the longitudinal and latitudinal directions are identified and removed. Further analysis is conducted on the residuals, accurately extracting the anomalous disturbance characteristics of the earthquake's precursor electric field, proving the method's
75 effectiveness.

2 Data and Methods

2.1 Study Area and Data Selection

A strong earthquake, with a magnitude of 7.6, struck the Tonga Islands (15.50°S, 174.50°W) on May 11, 2023, at 00:02 Beijing Standard Time (BST) and occurred at a depth of 200 km. According to the empirical formula for the lithospheric seismogenic
80 zone proposed by Dobrovolsky et al. (1979):

$$R = 10^{0.43M}, \tag{1}$$

in which 'M' represents the earthquake magnitude and 'R' represents the radius of the seismogenic zone in kilometers, the radius of the seismogenic zone for the Tonga Islands earthquake is determined to exceed 1,850 km. Consequently, the study area has been defined to encompass a region extending ± 20° from the earthquake's epicenter.

85   In this study, electric field data in the ELF band observed by the CSES-01 satellite were utilized. The orbital revisit period of the CSES-01 satellite is 5 days. The onboard Electric Field Detector (EFD) can observe ULF, ELF, VLF, and HF bands, generating three-component electric field time-series data and Power Spectral Density (PSD) data. For this study, the x-component of the electric field PSD was specifically selected.

   To date, the CSES-01 satellite has generated one of the most comprehensive datasets in the field of ionospheric electric field

90   observations. The CSES-01 satellite and its payload, both in good operating condition, have demonstrated strong performance in monitoring natural phenomena such as magnetic storms and seismic activity. Research has confirmed the high reliability of the satellite observations, yielding significant results, particularly in the validation of electric field data(Huang et al., 2023). These results have provided robust data support for scientific research and disaster prevention. In this study, observations from the night-side of the satellite were primarily utilized to enhance data quality. Night-time data exhibit smaller daily amplitude variations and

95   are more sensitive to sudden ionospheric disturbances.

2.2 Research Methodology

2.2.1 STL decomposition

   STL (Seasonal and Trend Decomposition using Loess) is a versatile and robust method for time series analysis. Developed by Cleveland et al. (1990), this method is based on Loess (Locally Weighted Scatterplot Smoothing). It is not only fast to compute

100   but also maintains its efficiency even for very long time series with extensive trend and seasonal smoothing. STL decomposes a time series into seasonal, trend, and residual components. The seasonal component captures regular, repeating patterns, the trend component indicates the underlying direction of the data, and the residual component represents irregular fluctuations.

   In a mathematical formulation, the data in a time series can be represented by the following Eq. (2):

$$y_t = S_t + T_t + R_t, \tag{2}$$

105   Where y_t is the data, S_t is the seasonal component, T_t is the trend component, and R_t is the residual component.

   The design of the STL decomposition is straightforward, offering several advantages. Firstly, it allows control over the rate of change of seasonality and the smoothness of the trend period—including monotonic seasonality—which enables optimal tailoring of the specificity of the time series being analyzed. Secondly, STL exhibits robustness to outliers. Even in the presence of missing values and outliers, these anomalies do not affect the estimation of the trend cycle and seasonal components(Sohrabbeig et al.,

110   2023). Consequently, these properties render STL particularly suitable for analyzing satellite data with large volumes.

2.2.2 Intensity Calculation

   STL decomposition, as a method of analyzing time-series data, can clearly identify the intensity of seasonal and trend changes. Based on the results of STL decomposition, the seasonal intensity F_S can be calculated using:

$$F_S = max\left(0, 1 - \frac{Var(R_t)}{Var(S_t + R_t)}\right), \tag{3}$$

Where F_S represents the intensity of the seasonal component, $Var(R_t)$ is the variance of the residual component, and $Var(S_t)$ is the variance of the seasonal component.

Similarly, the trend strength F_T can be calculated as follows:

$$F_T = max\left(0, 1 - \frac{Var(R_t)}{Var(T_t+R_t)}\right), \tag{4}$$

Where F_T represents the strength of the trend component and $Var(T_t)$ is the variance of the trend component.

$F_S(F_T)$ takes values from 0 to 1, with 0 representing the absence of seasonality (trend) in the time series, and values close to 1 indicating a significant seasonal (trend) component.

2.2.3 C-value

In previous studies, electromagnetic signals have been shown to exhibit fractal features in some ground-based ULF magnetic field data processing. Based on this, Zhang et al. (2010) proposed a method for identifying low-frequency electric field perturbations, defining an exponential relationship between the spectral data S_E and the frequency f using Eq. (5). The following Eq. (5) is used to identify low-frequency electric field perturbations:

$$S_E = a \cdot f^{-b}, \tag{5}$$

Further, Eq. (6) is constructed by logarithmically converting Eq. (5) and taking the absolute value, defining the function C:

$$C = a_0 + b \times |R|, \tag{6}$$

Where $a_0 = \lg a$. In applying this method, the parameters a, b, and the correlation coefficient R are extracted by fitting the spectral data S_E to the frequency f, and the value of C is calculated based on the result. The C-value is used in this study to measure the perturbation of the electric field power density (Huang et al., 2023).

3 Experimental Results

3.1 Satellite Data Analysis

STL decomposition, a method widely used for time series analysis, decomposes time series data into three components: seasonal, trend, and residual. The primary distinction between this study and prior applications of this method is the shift from predictive analyses to residual-based analysis of anomalous pre-seismic electric field perturbations. This approach eliminates conventional perturbations, thereby revealing or emphasizing unconventional perturbations associated with earthquakes. Additionally, utilizing the isolated seasonal and trend components allows the study of conventional perturbations that affect observed ionospheric effects and their underlying physical causes. Fig. 1 illustrates the STL decomposition results for the five-day revisit cycle that precedes the earthquake.
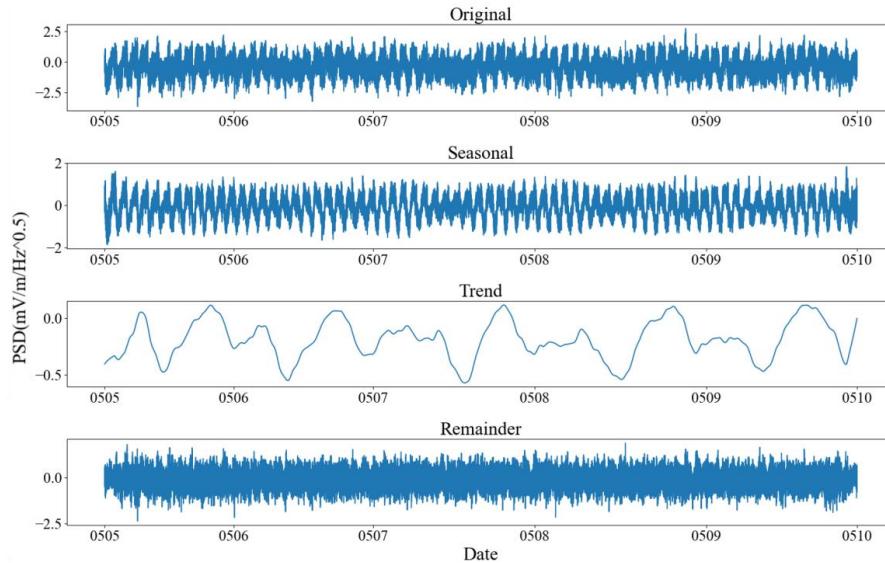
Figure 1: STL Decomposition Results from May 6 to May 10

The Original subplot in Fig. 1 presents the results of the original data after amplification and logarithmic processing, revealing
145   distinct dual-periodic fluctuations in the PSD. The Seasonal subplot illustrates the data's periodic trend, depicting periodic
changes in the longitudinal direction of the electric field. In the seasonal component, a stable cyclical trend that decreases and
then increases within a single orbit forms a V-shaped trend. The Trend subplot depicts the long-term trend of the data,
corresponding to variations between satellite orbits and representing periodic variations in the latitudinal component of the electric
field. This subplot distinctly shows a dual-peak trend with clear daily periodicity. The Remainder subplot displays the raw PSD,
150   subtracting the seasonal and trend components, and reveals the residual data that clearly retains the anomalous features suggested
by the data.

3.2 Analysis of Influencing Factors

Among the three components decomposed by STL, the seasonal and trend components both exhibit distinct periodicity.
Specifically, the seasonal component follows a single satellite orbit as a cycle, revealing variations in the electric field from 65°S
155   to 65°N latitude. As shown in Fig. 2, the seasonal component, decomposed from the night-side ascending orbit 29165, corresponds
to the first V-shaped trend of the seasonal component in Fig. 1 and is associated with an orbit within the 0°-50°E range in the
orbital projection of the PSD in Fig. 3. From the trend fitted by Loess, the value of the component decreases from 65°S, enters a
trough at about 40°S, rises near the equator, reaches a peak at about 30°N, then decreases slightly, and rises again. The spatial
distribution of the PSD in Fig. 3 corroborates this.
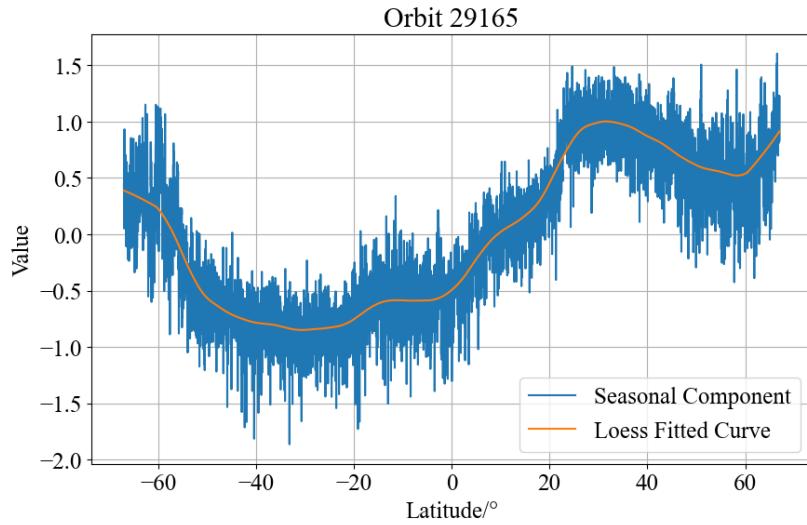
Figure 2: Seasonal Component Time Series for Orbit 29165 (Yellow Line Indicates Loess Fitting Results)
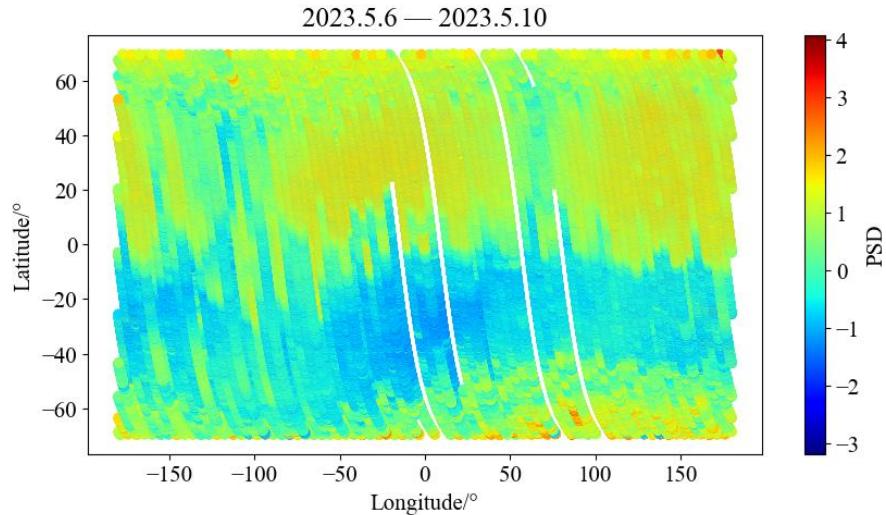
Figure 3: PSD Orbit Projection Map from May 6 to May 10

The seasonal intensity is determined to be 0.67 according to Eq. (3), which indicates that the seasonal component comprises a larger proportion of the overall time series perturbations. Specifically, the perturbation of the longitude term explains 67% of the total perturbations in the data. This observation suggests that the latitude effect significantly impacts ionospheric electric field fluctuations. The perturbations observed in the high latitude and equatorial regions are likely due to the ionospheric electric field being significantly influenced by interactions between the polar region's auroral current and magnetic field, and by the equatorial current band.

Given that the satellite orbits the Earth 15 times in a single day, with its orbital position continuously shifting westward, the latitudinal spacing between adjacent ascending or descending orbits is approximately 24°, resulting in a total daily shift of approximately 360°. Consequently, the dual-peak cyclic fluctuations in the trend component, observed daily, reflect variations

between successive orbits and meridional changes in the ionospheric electric field from east to west. The bimodal peak regions in the daily ascending and descending orbits in May are statistically summarized in Fig. 4, which presents the density

175 distribution of the peak-orbit data. Subplots (a) and (b) display the spatial density distribution of the first and second peaks of the ascending orbits, respectively; subplots (c) and (d) display the spatial density distribution of the first and second peaks of the descending orbits. The first peak of the ascending orbit is distributed over the American continent, with the highest data density near 60°W, indicating frequent peak occurrences at this location. The spatial distribution of the second peak of the ascending orbit is wider, spanning the eastern regions of Asia and Australia, as well as the western region of the Pacific Ocean,

180 with two high-frequency peak areas near 110°E and 160°E. The first peak of the descending orbit is located in the Pacific region, with a high-frequency peak area near 170°E. The second peak of the descending orbit is primarily located in Europe and Africa, with a wide range of high-frequency peak areas from 0° to 30°E. In addition, the spatial distribution of the peaks in the four subplots transitions from edge areas with lower frequency to high-frequency peak areas and then back to edge areas. The relationship between distribution frequency and longitude approximates a normal distribution. The peak distribution area shows

185 a high degree of overlap with the lightning aggregation areas, as illustrated in Fig. 5, which depicts the global distribution of lightning in May 2023.
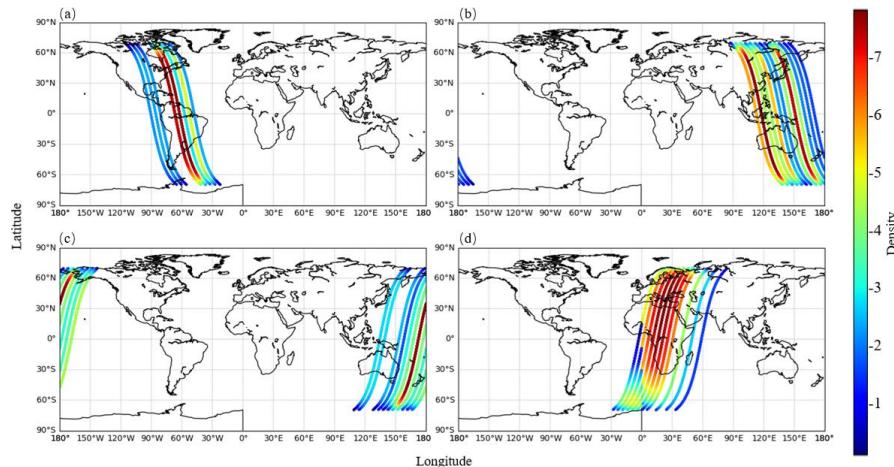
Figure 4: Spatial Distribution of Peaks in the Trend Component (Higher Density Values Indicate Higher Frequency of Peak Occurrences in the Region)
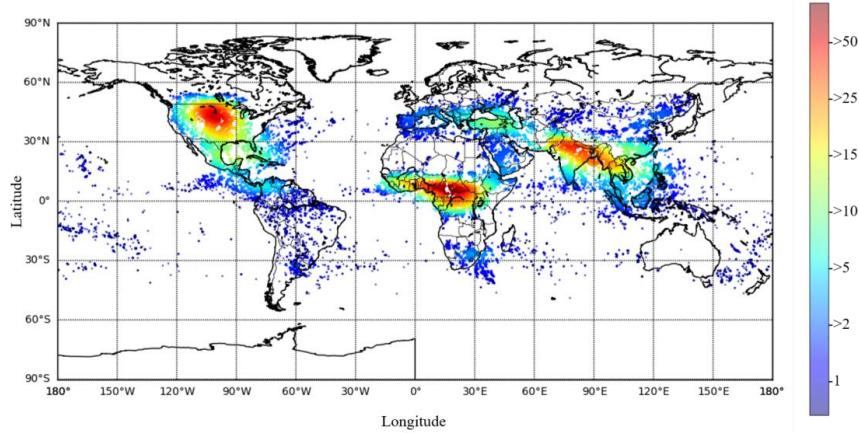
190

Figure 5: Global Lightning Distribution in May 2023

The calculated intensity of the trend component from Eq. (4) is 0.20, which indicates that the meridional perturbation attributable to the trend component represents 20 percent of all data perturbations. Given that lightning-dense regions impact the F layer of the ionosphere—where satellites are positioned—through mechanisms including electromagnetic pulses, atmospheric electric
195 field changes, gravity waves, and ionochemical reactions, it is hypothesized that the peak of the disturbance in the trend component could be attributed to high-density lightning.

The sum of the seasonal and trend strengths is 0.87, indicating that a majority of the time series fluctuations are decomposed into periodic regular perturbations. Furthermore, this suggests that the STL decomposition algorithm possesses significant explanatory power for the satellite data. The residuals mainly capture random noise and anomalous disturbances, which comprise only a minor
200 portion of the data. These perturbations become more pronounced upon removal of the significant periodic components associated with latitude and longitude coordinates. By eliminating prevalent disturbances in the ionospheric electric field, the residuals now more closely align with the assumption of randomness. Consequently, when anomaly detection algorithms are applied to the residual data, enhanced performance is anticipated.

3.3 Case Study of Earthquakes

205 Prior to extracting information about the anomalous perturbations associated with seismic precursors, it is essential to consider the spatial perturbation factors within the studied time period. The effects of the Kp and Dst indices on magnetic storm activity both before and after the earthquake are illustrated in Fig. 6. The results indicate that strong magnetic storms—characterized by a Dst value less than -200 and a Kp greater than 8—occurred on April 23-24, while moderate magnetic storms—with a Dst value less than -50 and a Kp greater than 4—occurred on May 6 and May 20.
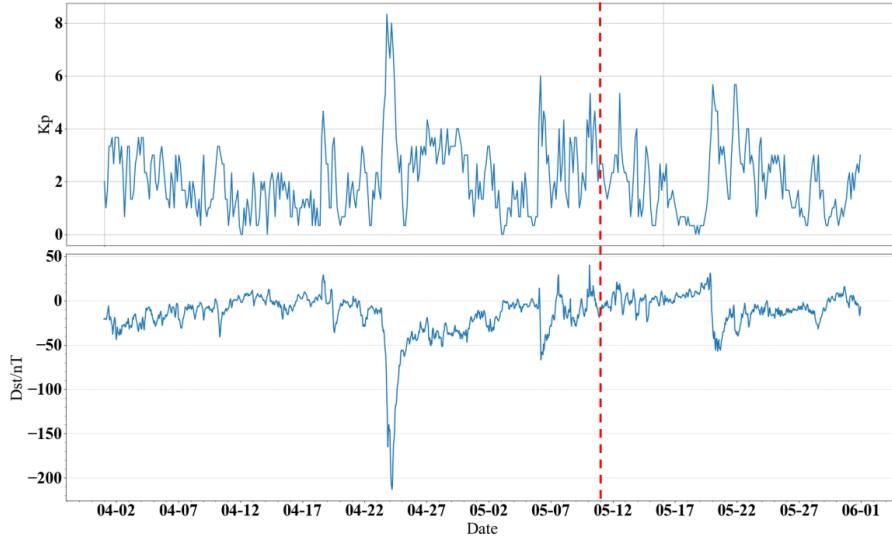
210

Figure 6: Variations in Kp and Dst Indices from April 1 to May 31, 2023 (Red Dashed Line Indicates the Time of Earthquake Occurrence)

To analyze the unconventional perturbation information embedded in the power density residuals and to extract electric field perturbation features associated with earthquakes, an STL decomposition of the PSD values across multiple frequencies is initially performed to obtain the PSD residuals for each frequency. Subsequently, the residual values and frequencies are fitted
215 to the parameters a and b, and correlation coefficients R, as delineated in Eq. (5). Finally, the C-values are calculated as per Eq.

(6).
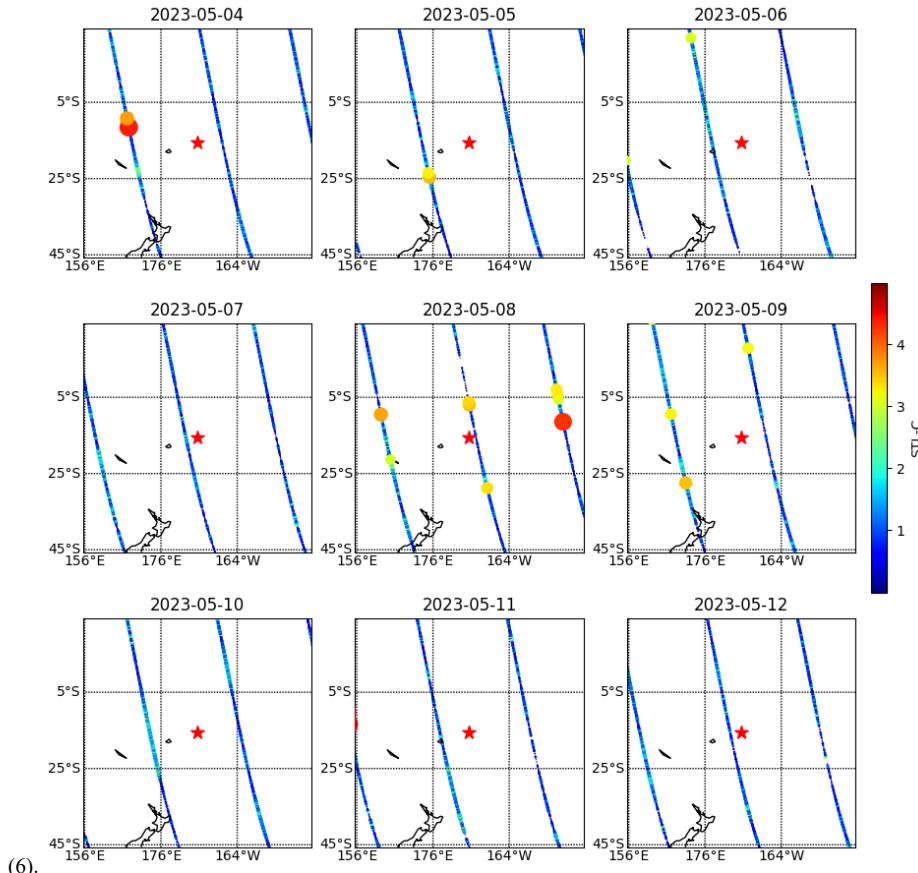
Figure 7: STL-C Variation Characteristics within the Seismic Region Before and After the Mw7.6 Tonga Islands Earthquake on May 11, 2023 (Red Star Indicates Epicenter Location)

Electric field power spectrum data collected by the CSES-01 satellite before and after the Mw 7.6 earthquake in the Tonga Islands on May 11, 2023, were processed and analyzed. The period spanning seven days before to one day after the earthquake (May 4-12, 2023) was selected for the study. As illustrated in Fig. 7, on May 4, the C-value exhibited an anomaly in the northwestern region of the seismogenic zone, reaching a peak of 4.4. On May 5, the C-value in the southwestern region declined slightly to 3.5. On May 6 and 7, the highest C-value further decreased to 2.5, indicative of a low-level state. On May 8 and 9, anomalies were observed in various directions near the center of the seismogenic zone, with the highest C-value rising above 3.5. On May 10, the day before the earthquake, the C-value dropped to 2.5. No significant changes were observed on the day of the earthquake or in the days following, indicating a return to a stable electric field state. This pattern suggests an anomalous increase in the C-value prior to the earthquake, indicating a discernible trend in the extreme values.

Fig. 8 depicts the temporal variation characteristics of the C-value maxima in the seismogenic zone from 40 days before the earthquake to 15 days after the earthquake. The anomalous disturbance, characterized by a C-value greater than 3.5, first appeared on April 21 (20 days before the earthquake) and was of short duration. The disturbance re-emerged from April 28 to April 30 (13-11 days before the earthquake), lasting three days, with the C-value maxima reaching 3.9 and a disturbance amplitude approximately two times the standard deviation. On May 4 (7 days before the earthquake), the maximum C-value rose to 4.4, the highest value in the two months before and after the earthquake, with a perturbation amplitude approximately three times the standard deviation. The perturbation amplitude then declined from May 5 to May 7 (6-5 days before the earthquake), rebounded

on May 8 (4 days before the earthquake) with a maximum C-value of 3.5 for two days, and stabilized at a relatively low level on May 10 (1 day before the earthquake). After the earthquake on May 11, the electric field remained stable.
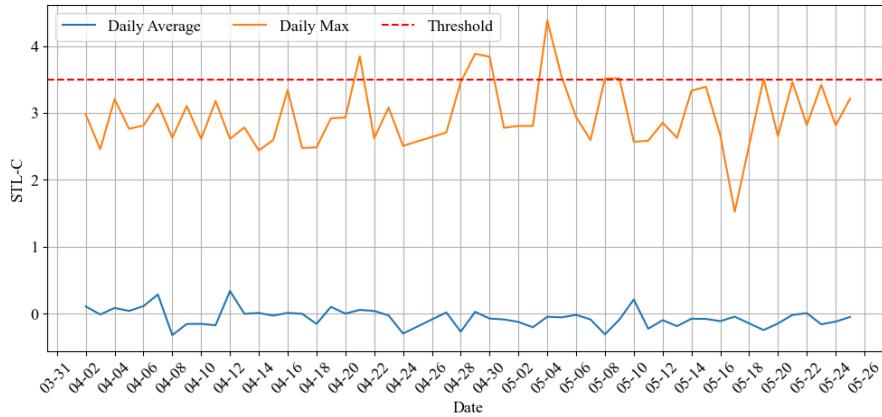
Figure 8: Variation Characteristics of STL-C Maximum and Average Values from April 1 to May 26, 2023

4 Discussion and Conclusion

4.1 Discussion

In this study, we utilize the latitude and longitude components decomposed by STL to investigate the periodic disturbances impacting the ionospheric effects observed in satellite data. Additionally, we analyze the ionospheric effects before and after earthquakes using residual data obtained by removing these disturbances. Excluding the effect of conventional disturbances in the ionospheric electric field renders the information about earthquake precursor anomalies in the data more pronounced. This exclusion also enables unconventional anomalous disturbances to emerge more prominently over a longer time scale. The results indicate that several significant anomalous disturbances in the ionospheric electric field were observed by the CSES-01 satellite during the 20 days preceding the Mw 7.6 earthquake in the Tonga Islands on May 11, 2023. The spatial and temporal distributions of these anomalous disturbances display a distinct pattern.

The seasonal and trend components of the STL decomposition of the electric field data respectively reflect the longitudinal and latitudinal variations of the ionospheric electric field. These components reveal a V-shaped periodic trend from south to north and periodic bimodal fluctuations from east to west in the satellite observation data. The seasonal component, which has a period corresponding to a single satellite orbit, is markedly influenced by latitudinal effects. In high-latitude regions, interactions with auroral currents and the magnetic field substantially influence the ionospheric electric field. In equatorial regions, factors including the equatorial electrojet among others, contribute to the seasonal component, thereby influencing the ionospheric electric field. The cyclic bimodal fluctuations of the trend component daily reflect changes in the electric field's latitudinal direction from orbit to orbit. A comparison of the bimodal peak distribution with global lightning distribution indicates a significant overlap between regions of high-density lightning and the distribution of the trend wave. This suggests that lightning profoundly influences the ionospheric F-layer through mechanisms such as electromagnetic pulses, changes in the atmospheric electric field, gravity waves, and ionochemical reactions, resulting in partial perturbations of the wave peaks in the trend component.

The calculated seasonal strength of 0.67 and trend strength of 0.20 suggest that 87% of the data fluctuations in variance can be attributed to conventional perturbations. Thus, seismic precursor information needs only to be extracted from the remaining 13% of unconventional perturbations, which significantly reduces the interference with the observed seismic ionospheric effects. After the removal of the seasonal and trend components, characteristics of the anomalous perturbations in the pre-seismic electric field

265 are extracted from the residual fraction. The C-values, computed according to Eq. (5) and Eq. (6), indicate the strength and variability of these anomalous perturbations. During the studied period, especially in the week before the earthquake, several significant anomalies in the C-values were noted. The highest value reached 4.4, with a perturbation amplitude of three times the standard deviation, substantially higher than that observed during the quiet period before the earthquake. Moreover, the STL algorithm's nature ensures that global or large-scale perturbations are generally captured in the trend or seasonal components,

270 whereas the residuals predominantly contain local or random anomalous perturbations. Consequently, geophysical events such as magnetic storms, which alter the global ionospheric electric field, are filtered out of the residuals, facilitating the identification and extraction of earthquake precursor information from the residuals.

4.2 Conclusion

By analyzing the PSD data observed by the CSES-01 satellite before and after the Mw 7.6 earthquake in the Tonga Islands

275 on May 11, 2023, the study found that:

The seasonal and trend components of the electric field data, decomposed using STL, respectively reflect changes in the longitudinal and latitudinal directions of the ionospheric electric field. They reveal the electric field's double periodicity, characterized by a V-shape from south to north and a bimodal shape from east to west. The variance of these periodic conventional perturbations accounts for 87% of the total data perturbations. Thus, only the remaining 13% of unconventional perturbations are

280 needed to extract seismic precursor information, significantly reducing observational interference.

Anomalous perturbations implied in the residual component are more readily extracted after the removal of conventional perturbations. Anomalous perturbations associated with the Tonga Islands Mw 7.6 earthquake first appeared 20 days prior to the event. In the week preceding the earthquake, the C-value displayed significant anomalies several times, and the magnitude of the perturbations reached three times the standard deviation, recovering to normal levels the day before the event.

285 The STL decomposition algorithm demonstrates robust capability in interpreting satellite data and can effectively isolate disturbances of varying directions and causes in the ionospheric electric field, thereby shielding against global disturbances such as magnetic storms. The longitudinal component obtained from the decomposition highlights the latitudinal effects on the ionospheric electric field. Meanwhile, the distribution area of the spatial location of the bimodal peaks of the latitude component closely aligns with the lightning congregation areas, potentially due to changes in the ionospheric electric field induced by

290 lightning.

Competing interests

The contact author has declared that none of the authors has any competing interests.

Author contribution

Jianping Huang and Zhong Li were responsible for the conceptualization, supervision, and project administration. Junjie Song,

295 Wenjing Li, and Hengxin Lu contributed to methodology development, data analysis, and drafting the manuscript. Xingsu Li and Yumeng Huo were in charge of software development and data curation. Ruiqi Yang participated in experiment validation and visualization. All authors contributed to the review and editing of the manuscript.

Acknowledgments

This work made use of data from the CSES mission, a project funded by China National Space Administration(CNSA) and China

300   Earthquake Administration (CEA). This work was supported by National Key R&D Program of intergovernmental cooperation in science and technology (Grant No. 2023YFE0117300), the International Space Science Institute (ISSI in Bern, Switzerland and ISSI-BJ in Beijing, China), supporting International Team 23-583 led by Dedalo Marchetti and Essam Ghamry, Hebei Province Graduate Professional Degree Excellent Teaching Case (Library) Construction Project (No. KCJPZ2023060). We acknowledge the CSES Scientific Mission Center for Providing Data (The English version of https://www.leos.ac.cn/).

305   **References**

Astafyeva, E., Shalimov, S., Olshanskaya, E., & Lognonné, P.: Ionospheric response to earthquakes of different magnitudes: Larger quakes perturb the ionosphere stronger and longer. Geophys. Res. Lett., 40(9), 1675-1681. doi:10.1002/grl.50398, 2013.

Chen, W., Marchetti, D., Zhu, K., Sabbagh, D., Yan, R., Zhima, Z., Shen, X., Cheng, Y., Fan, M., Wang, S., Wang, T., Zhang, D., Zhang, H., & Zhang, Y.: CSES-01 Electron Density Background Characterisation and Preliminary Investigation of Possible Ne

310   Increase before Global Seismicity. Atmosphere, 14(10), 1527. doi:10.3390/atmos14101527, 2023.

Chmyrev, V. M., Berthelier, A., Jorjio, N. V., Berthelier, J. J., Bosqued, J. M., Galperin, Y. I., Kovrazhkin, R. A., Beghin, C., Mogilevsky, M. M., Bilichenko, S. V., & Molchanov, O. A.: Non-linear Alfven wave generator of auroral particles and ELF/VLF waves. Planet. Space Sci., 37(6), 749-759. doi:10.1016/0032-0633(89)90044-5, 1989.

Cleveland, R. B., Cleveland, W. S., McRae, J. E., & Terpenning, I.: STL: A seasonal-trend decomposition. J. off. Stat, 6(1), 3-73.

315   1990.

Dobrovolsky, I. P., Zubkov, S. I., & Miachkin, V. I.: Estimation of the size of earthquake preparation zones. Pure Appl. Geophys., 117(5), 1025-1044. doi:10.1007/bf00876083, 1979.

Elliott, T., & Su, Z. (2020). iNZightTS: Time Series for 'iNZight'. Retrieved from: http://dx.doi.org/10.32614/cran.package.inzightts

320   Gokhberg, M. B., Morgounov, V. A., Yoshino, T., & Tomizawa, I.: Experimental measurement of electromagnetic emissions possibly related to earthquakes in Japan. J. Geophys. Res.: Solid Earth, 87(B9), 7824-7828. doi:10.1029/jb087ib09p07824, 1982.

Huang, J., Li, Z., Li, Z., Li, W., Conti, L., Lu, H., Zhou, N., Han, Y., Liu, H., Chen, X., Chen, Z., Song, J., & Shen, X.: Automatic Identification and Statistical Analysis of Data Steps in Electric Field Measurements from CSES-01 Satellite. Remote Sens., 15(24), 5745. doi:10.3390/rs15245745, 2023.

325   Huang, J., Zhang, F., Li, Z., Shen, X., Yang, B., Li, W., Zeren, Z., Lu, H., & Tan, Q.: Disturbance identification of electric field data observed by the CSES-01 satellite before earthquakes. Science China Earth Sciences, 66(8), 1814-1824. doi:10.1007/s11430-022-1048-8, 2023.

Larkina, V. I., Maltseva, O. A., & Molchanov, O. A.: Satellite observations of signals from a Soviet mid-latitude VLF transmitter in the magnetic-conjugate region. J. Atmos. Terr. Phys., 45(2-3), 115-119. doi:10.1016/s0021-9169(83)80015-4, 1983.

330   Leonard, R. S., & Barnes, R. A.: Observation of ionospheric disturbances following the Alaska earthquake. J. Geophys. Res., 70(5), 1250-1253. doi:10.1029/jz070i005p01250, 1965.

Li, Z., Yang, B., Huang, J., Yin, H., Yang, X., Liu, H., Zhang, F., & Lu, H.: Analysis of Pre-Earthquake Space Electric Field Disturbance Observed by CSES. Atmosphere, 13(6), 934. doi:10.3390/atmos13060934, 2022.

Marchetti, D., De Santis, A., Shen, X., Campuzano, S. A., Perrone, L., Piscini, A., Di Giovambattista, R., Jin, S., Ippolito, A.,

335   Cianchini, G., Cesaroni, C., Sabbagh, D., Spogli, L., Zhima, Z., & Huang, J.: Possible Lithosphere-Atmosphere-Ionosphere Coupling effects prior to the 2018 Mw = 7.5 Indonesia earthquake from seismic, atmospheric and ionospheric data. J. Asian Earth Sci., 188, 104097. doi:10.1016/j.jseaes.2019.104097, 2020.

Martucci, M., Bartocci, S., Battiston, R., Burger, W. J., Campana, D., Carfora, L., Conti, L., Contin, A., De Donato, C., De Santis, C., Follega, F. M., Iuppa, R., Marcelli, N., Masciantonio, G., Mergè, M., Oliva, A., Osteria, G., Palma, F., Parmentier, A., Perfetto,

340   F., Picozza, P., Pozzato, M., Ricci, E., Ricci, M., Ricciarini, S. B., Sahnoun, Z., Scotti, V., Sotgiu, A., Sparvoli, R., Vitale, V., Zoffoli, S., & Zuccon, P.: New results on protons inside the South Atlantic Anomaly, at energies between 40 and 250 MeV in the period 2018–2020, from the CSES-01 satellite mission. Physical Review D, 105(6). doi:10.1103/physrevd.105.062001, 2022.

Pulinets, S., Davidenko, D., & Pulinets, M.: Atmosphere-ionosphere coupling induced by volcanoes eruption and dust storms and role of GEC as the agent of geospheres interaction. Adv. Space Res., 69(12), 4319-4334. doi:10.1016/j.asr.2022.03.031, 2022.

345 Sarkar, S., Gwal, A. K., & Parrot, M.: Ionospheric variations observed by the DEMETER satellite in the mid-latitude region during strong earthquakes. J. Atmos. Sol. Terr. Phys., 69(13), 1524-1540. doi:10.1016/j.jastp.2007.06.006, 2007.

Serebryakova, O. N., Bilichenko, S. V., Chmyrev, V. M., Parrot, M., Rauch, J. L., Lefeuvre, F., & Pokhotelov, O. A.: Electromagnetic ELF radiation from earthquake regions as observed by low-altitude satellites. Geophys. Res. Lett., 19(2), 91-94. doi:10.1029/91gl02775, 1992.

350 Shen, X., Zhang, X., Yuan, S., Wang, L., Cao, J., Huang, J., Zhu, X., Piergiorgio, P., & Dai, J.: The state-of-the-art of the China Seismo-Electromagnetic Satellite mission. Sci. China Technol. Sci., 61(5), 634-642. doi:10.1007/s11431-018-9242-0, 2018.

Silina, A. S., Liperovskaya, E. V., Liperovsky, V. A., & Meister, C. V.: Ionospheric phenomena before strong earthquakes. Nat. Hazards Earth Syst. Sci., 1(3), 113-118. doi:10.5194/nhess-1-113-2001, 2001.

Sohrabbeig, A., Ardakanian, O., & Musilek, P.: Decompose and Conquer: Time Series Forecasting with Multiseasonal Trend
355 Decomposition Using Loess. Forecasting, 5(4), 684-696. doi:10.3390/forecast5040037, 2023.

Sokolov, S. N.: Magnetic storms and their effects in the lower ionosphere: Differences in storms of various types. Geomag. Aeron., 51(6), 741-752. doi:10.1134/s0016793211050124, 2011.

Zhang, X., Battiston, R., Shen, X., Zeren, Z., Ouyang, X., Qian, J., Liu, J., Huang, J., & Miao, Y.: Automatic Collecting Technique of Low Frequency Electromagnetic Signals and Its Application in Earthquake Study. In Lect. Notes Comput. Sci. (pp. 366-377):
360 Springer Berlin Heidelberg, 2010.

Zhima, Z., Yan, R., Lin, J., Wang, Q., Yang, Y., Lv, F., Huang, J., Cui, J., Liu, Q., Zhao, S., Zhang, Z., Xu, S., Liu, D., Chu, W., Zhu, K., Sun, X., Lu, H., Guo, F., Tan, Q., Zhou, N., Yang, D., Huang, H., Wang, J., & Shen, X.: The Possible Seismo-Ionospheric Perturbations Recorded by the China-Seismo-Electromagnetic Satellite. Remote Sens., 14(4), 905. doi:10.3390/rs14040905, 2022.